Journal of
Marine Science and Engineering

MDPI

Article

Using Video Monitoring to Test a Fetch-Based Aeolian Sand Transport Model

Pam Hage *, Gerben Ruessink, Zilla van Aartrijk and Jasper Donker

Department of Physical geography, Faculty of Geosciences, Utrecht University, 3508TC Utrecht, The Netherlands; B.G.Ruessink@uu.nl (G.R.); Z.E.M.vanAartrijk@students.uu.nl (Z.v.A.); jasper.donker@geodan.nl (J.D.)

* Correspondence: pamhage@hotmail.com

Received: 18 December 2019; Accepted: 7 February 2020; Published: 12 February 2020

Abstract: Transport of beach sand to the foredune by wind is essential for dunes to grow. The aeolian sand transport rate is related to wind velocity, but wind-based models often overpredict this transport for narrow beaches (<100 m). To better predict aeolian sand transport, the fetch-based Aeolus model was developed. Here, we qualitatively test this model by comparing its transport-rate output to visual signs of aeolian transport on video imagery collected at Egmond aan Zee, the Netherlands, during a six-month winter period. The Aeolus model and the Argus images often agree on the timing of aeolian transport days, except when transport is small; that is not always visible on the Argus images. Consistent with the imagery (minimal signs of aeolian activity in strong winds), the Aeolus model sometimes predicts the actual transport to be smaller than the potential transport. This difference is largest when wind velocity is large, and its direction is cross-shore. Although transport limitations are not predicted to be common, the results suggest that their effect on the total transport in the study period was substantial. This indicates that the fetch distance should be taken into account when calculating aeolian transport for narrow beaches on longer timescales (>weeks).

Keywords: aeolian sand transport; aeolus model; video monitoring; beach processes; transport conditions

1. Introduction

Coastal dunes are dynamic systems whose evolution is determined by aeolian and marine processes, the presence of vegetation, and human activities. Storms are responsible for dune erosion, a process lasting a few hours or days, while dune recovery and growth are driven primarily by the wind, a process that can take months to years. Time-averaged aeolian transport models often use only grain size and wind shear velocity [1–4]. This provides good results under controlled conditions, with a dry, horizontal surface, uniform grain size and steady wind, but transport on a natural beach is also affected by, for example, the moisture content of the sand, the beach slope, the bed roughness, and wind deflection by the foredune (e.g., [2,3,5–13]). The computed volume of wind-blown sand often exceeds the volume deposited on the foredune, with the latest reaching values as small as 15% of the former when the beach is narrow [2,10–12,14,15].

Aeolian sand transport has a clear visual signal, as the transported sand organizes itself as streamers, which are elongated features of saltating grains with a strong spatial and temporal variability [16,17], and sand strips, which are slipfaceless bedforms [18–20] with a wavelength of around 10 m and a migration velocity of a few meters per hour [21]. Ref. [22] observed that strong winds do not necessarily result in large amounts of aeolian transport and/or the presence of aeolian bedforms. A similar mismatch was also observed by [23], who found that small wind velocities (≈8 m/s), and therefore small potential aeolian transport rates, can nonetheless cause sand strips

to cover the beach. According to these studies, a short fetch, i.e., the distance over which the wind blows over the beach, and a large surface moisture content form important limitations for aeolian sand transport. For arctic beaches, ice and snow cover form limiting factors as well [22], while nourished beaches may have reduced aeolian transport because of shell lag deposits [24].

To improve the prediction of aeolian sand transport on narrow beaches, ref. [3] proposed a series of spatially explicit equations that include fetch distances. In addition to the fetch itself, they considered the maximum possible fetch and a critical fetch, which is the downwind distance needed for aeolian sand transport to reach its (potential) maximum. When the critical fetch is longer than the maximum fetch, the maximum transport rate cannot be reached, and transport will be limited. The modelling framework does not predict a quantitative transport rate, but it is a conceptual model capable of calculating the spatial distribution of a relative sand transport rate as a function of the critical fetch distance, beach geometry, and wind angle. The model was tested with data from a 9-month field campaign at Greenwich Dunes, Canada, by [25] and further extended to be able to calculate sand transport for limited transport conditions. The model of [25] forms the basis of this research and extracts a beach width and uniform moisture content for the beach from video imagery. The model applies several filter steps to select events likely to have transport. All events where no transport to the dunes is expected are ignored: the wind must be above the threshold of sand entrainment and have an onshore component, the gravimetric moisture content of the beach must be below 10%, the beach should not be fully inundated, and ice and snow should not cover more than half the beach. Then the critical fetch distance is determined from the wind velocity and increased with moisture content, making it more likely that it will exceed the maximum fetch (causing limited transport) when the beach is moist. Limited transport events will have a smaller transport rate, depending on the ratio between the critical and maximum fetch. It was found that for the studied period at Greenwich Dunes, the total transport rate was almost 29 times larger than the measured transport amount when only wind direction and entrainment threshold were used as a filter. This diminished to a factor 11.8 when the filter for snow cover, >10% moisture content, and an inundated beach were used. Including the effect of fetch diminished it further to a factor 8.2, and when the full model was used, this became to 6.2 times the measured transport amount. The improved predictions for transport show the feasibility of the fetch-approach, but the strong dependence on video data makes this model hard to apply to unmonitored coastal sites.

In this paper, we extend [25]'s work with a new fetch-based model, called Aeolus, which uses time series of seawater elevation to determine groundwater cross-shore variability depth, which in turn determines a spatially and temporally varying surface moisture content. Furthermore, the Aeolus model determines the width of the beach, which is needed for calculating fetch distances, from a given bed profile, wind, water level, and wave data. Here, we aim to qualitatively test the Aeolus model for long time scales (months) by comparing its results to visual signs of aeolian sand transport at the narrow beach of Egmond aan Zee, the Netherlands, previously explored in [21,23]. The predicted transport will be compared with visual signs of aeolian transport, as determined from video monitoring. In particular, we are interested to see if the model can provide a better match between predicted and visually observed transport than a wind-alone model. The methodology is introduced in Section 2, including a description of the Aeolus model, field site, video monitoring data, model set-up and synthetic runs. Section 3 describes our results. The discussion and conclusion can be found in Sections 4 and 5, respectively. A quantitative test of the model is left for future work.

2. Methodology

2.1. Model Description

The Aeolus model consists of three modules. The first module is a groundwater model that uses the non-linear Boussinesq equation for finite-amplitude water table fluctuations (e.g., [26]) with a spatially constant aquifer thickness D. The Boussinesq equations follows from the substitution of

Darcy's Law into the continuity equation [27]. Here, the Boussinesq equation is extended to include infiltration by wave run-up, as proposed by [28,29]. The groundwater model assumes that the sand is homogeneous and isotropic, and that groundwater flow is essentially horizontal, which is common for sandy beaches [26]. The cross-shore (x) and temporal (t) evolution of the water table height η (m) with respect to Mean Sea Level (MSL) is then

$$\frac{\partial \eta(x,t)}{\partial t} = \frac{K}{n_e}\frac{\partial}{\partial x}\{[D+\eta(x,t)]\frac{\partial \eta(x,t)}{\partial x}\} + \frac{U_l}{n_e} \quad (1)$$

where K is the hydraulic conductivity of the beach (m/s), n_e is the effective porosity (-), and U_l is the run-up infiltration flow rate (m/s). U_l can be written as [28,30]

$$U_l = \begin{cases} C_l K f(x), & \text{if } x_{cf} \le x \le x_{ru} \\ 0, & \text{otherwise} \end{cases} \quad (2)$$

where C_l is an infiltration coefficient (-) and $f(x)$ is a function of x (-). x_{cf} is the location where the depth of the water table equals the thickness of the capillary fringe, and x_{ru} is the maximum run-up location. Following [30], we let $f(x)$ increase linearly from 0 at x_{cf} to 1 at x_{ru}. The typical thickness for the capillary fringe on a sandy beach is 0.1 to 0.2 m [31]. The parametrization by [32] was adopted to compute x_{ru}. Refs. [30,33] mention the importance of wave run-up for accurately predicting $\eta(x,t)$ above the high-tide level, especially when waves are energetic.

Equation (1) was solved numerically, as described by [30], with a centered finite difference method in space and a fourth-order Runge–Kutta integration technique in time. The seaward boundary condition is a moving shoreline at location $x_{sh}(t)$ with elevation $\eta_{sh}(t)$

$$\eta_{sh}(x_{sh},t) = \zeta_0(t) + \xi_{sh}(t) \quad (3)$$

It consists of the offshore water level $\zeta_0(t)$ and the wave set-up $\xi_{sh}(t)$, estimated with offshore wave data and the parametrization of [32]. The imposed landward boundary is $\partial\eta/\partial x = 0$. The beach profile must be monotonically increasing to apply Equation (1), meaning that intertidal sandbars and troughs cannot be present. This part of the model needs a spin up time of approximately a month to dampen and stabilize the strong fluctuations in the groundwater.

The second part of the model determines the surface soil moisture of the beach. It is assumed that the moisture profile above the water table is in hydrostatic equilibrium, meaning that the rising and falling of the water table with time do not change the profile shape. The surface moisture thus responds immediately to changes in the groundwater level. These assumptions are discussed in, for example, Refs. [30,34], who argued that these assumptions are realistic unless the beach sand is rather fine (≈150 µm). By adopting the water retention curve by [35], the gravimetric surface moisture content w_s can be related to the groundwater depth h as

$$w_s = w_{res} + \frac{w_{sat} - w_{res}}{[1+(\alpha|h|)^n]^{1-1/n}} \quad (4)$$

where w_{sat} is the saturated water content (-), w_{res} is the residual water content (-), and n is a measure of the pore-size distribution (-). α (m^{-1}) is related to the inverse of the air entry suction and affects the thickness of the capillary fringe.

The third module is based on the conceptual aeolian fetch model of [3], as extended by [25]. Ref. [3] proposed a parametrization of the increase in the aeolian transport rate q with downwind fetch distance F, with q the product of the potential transport rate q_p and a trigonometric function. According to [36], the following function fits best with observations from agricultural fields

$$q(F) = min\left[q_p, q_p \times \sin\left(\frac{\pi}{2}\frac{F}{F_c}\right)\right] \quad (5)$$

In [36], F_c depends positively on wind speed U as $F_c = 4.38\ U - 8.23$, and the computed value of F_c is then modified based on w_s. In [36], w_s and the F_c modification are spatially constant. If w_s is less than 4%, F_c remains unchanged. If w_s is between 4% and 6%, F_c increases with a factor 1.5, and if w_s is between 6 and 10%, F_c is 1.75 times as large compared to the dry-sand F_c. No transport is calculated if w_s is above 10%. In the Aeolus model, w_s varies in the cross-shore direction, which implies that F_c is spatially varying too. Therefore, Equation (5) was adapted into a spatially forward-stepping equation

$$q(i) = \begin{cases} min\left[q_p, q(i_1 - 1) + q_p \times \sin\left(\frac{\pi}{2}\frac{F(i)}{F_c(i)}\right)\right], & \text{if } w_s(i) \leq w_{s,max} \\ 0, & \text{otherwise} \end{cases} \quad (6)$$

where i are spatial indices. When the most seaward gridpoint has a value less than the threshold value $w_{s,max}$ set by the user, the computation of q starts. The remaining values for $w_s(x)$ are rounded to multiples of 0.5% (now referred to as w_s'). The fetch is the downwind distance over which the surface moisture is constant, starting one spatial gridpoint upwind of the most upwind gridpoint of a group of gridpoints with equal w_s'. This is indicated in Equation (5) with the $i_1 - 1$ index. i thus refers to all locations with constant w_s'. This approach causes F to reset to 0 with every change in w_s'. To avoid F resetting for even tiny changes in w_s, w_s was rounded to multiples of 0.5%.

The critical fetch in Aeolus is computed at each grid point as

$$F_c(i) = p(w_s') * [4.38U - 8.23] \quad (7)$$

Based on the work of [5], $p = 1$ for $w_s' \leq 4\%$ and a 0.125 increase in p per 1% increase in moisture. q in Equation (6) is computed up and including the transition from beach to dune, which occurs at elevation z_{up}, a user-specified value. We refer to q at z_{up} as the actual aeolian transport rate q_a.

The potential transport rate q_p (kg m^{-1} s^{-1}) is here computed following [2,37] as

$$q_p = 0.1 \times [-0.47 + 4.97 D_{mm}] \times 10^{-4} \left(\frac{\alpha_{Hsu} U}{\sqrt{g D_{cm}}}\right)^3 \quad (8)$$

where U is the time-averaged (over 10 to 60 min) wind velocity measured at a height of 2 to 10 m. As in [1], the grain size has to be specified in mm for D_{mm} and cm for D_{cm} and $g = 981$ cm/s^2. The parameter α_{Hsu} relates U to the shear velocity U_* in cm/s can be determined with

$$\alpha_{Hsu} = \frac{100\kappa}{\log\left(\frac{z}{z_0}\right)} \quad (9)$$

where $\kappa = 0.41$ is Von Karman's constant, z is the height above the bed where the wind velocity is measured, and z_0 is the roughness length. Based on extensive measurements, Ref. [1] proposed $\alpha_{Hsu} = 4$.

2.2. Observations

2.2.1. Field Site

The study site is located south of Egmond aan Zee, the Netherlands (Figure 1). The straight coastline has an orientation of 7° east of north and consists of medium-fine sand with a median grain size of about 240 µm. The beach is exposed to waves from the southwest to the north [38]. The Dutch coast has a significant offshore wave period and height of 5 s and 1.2 m, respectively, which do not show strong alongshore differences. During storms, the significant offshore wave height can increase to over 5 m. Especially storms from the northwest are responsible for surges more than 1 m. As a result, the intertidal beach can be flooded for several days [39]. The mean wind speed is 5.8 m/s, based on wind data from 1981 to 2010 measured at de Kooy, 40 km north of the field site [40]. During storms, U

can attain values up to 30 m/s. The dominant wind direction at the site is south-southwest (210°–230° with respect to north).

The semi-diurnal tide ranges from 1.4 m (neap tide) to 1.8 m (spring tide) and affects the width of the beach, which usually varies between 30 and 100 m. The intertidal beach usually has one or two slipface bars [41–43]. The high foredune (20 to 25 m) has a steep seaward front (40°–50°) due to occasional erosion events [44]. Large parts of the dune are covered in European marram grass (*Ammophila arenaria*), especially at heights exceeding 10 to 15 m above beach level. During prolonged periods of time without surges, embryo dunes can develop at the base of the foredune [45].

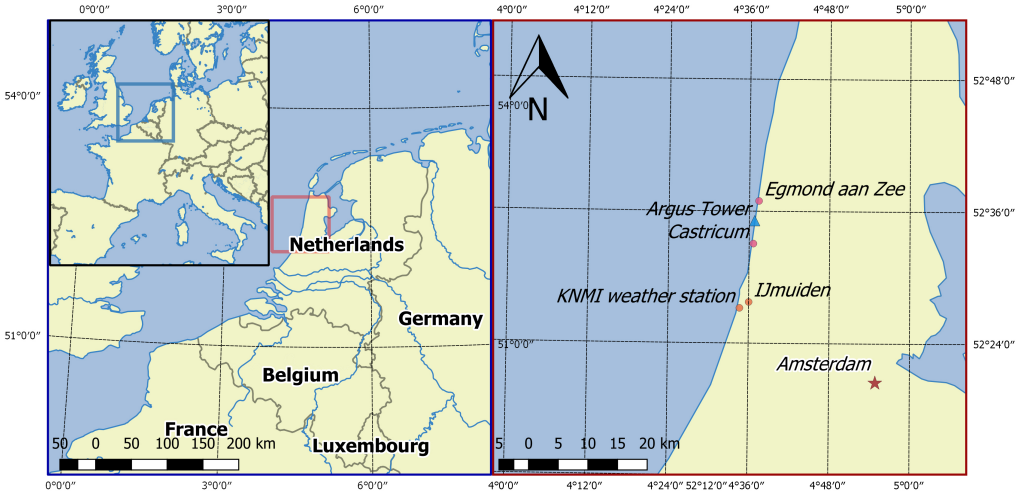

Figure 1. Map of the field site and weather station.

2.2.2. Video Monitoring

The beach south of Egmond aan Zee was monitored with an Argus video system [46] between April 1998 and October 2015. Argus is an optical remote sensing system pioneered by Holman and Sallenger [47] for sampling the nearshore environment. An Argus system consists of a suite of cameras at the top of a high structure to gain an unhindered view of the beach. A timing module is installed to ensure a synchronized collection of the images [48]. The Argus system at Egmond aan Zee consisted of five RGB-color cameras, which were mounted on a 45-m high tower on the upper beach. The cameras provided an 180° view, from south-southwest to north-northeast with a resolution of 640 × 480 pixels from 1998 to February 2004, 1024 × 768 pixels from 2004 to August 2005 and 1392 × 1040 pixels until 2015. Every 30 min, each camera produced three different oblique images: a snapshot, a time-exposure (timex) and a variance image. Only the first two types of images are used in this research. The timex images were created by images taken with a frequency of 2 Hz over a 10-min period. This procedure blurs out all movement in the 10-min time frame, such as individual waves breaking on the subtidal bars and aeolian streamers on the beach. The movement of streamers is thus best noticeable when a snapshot and timex of the same hour are compared: an active streamer can be seen on a snapshot image, but not on a timex image (Figure 2). This makes them stand out from immobile, small, irregular patches of dry sand that look like streamers on a snapshot image. Both snapshot and timex image can be used to determine the movement of aeolian bedforms called sand strips (Figure 2), but as sand strips move relatively slowly (a few meters per hour [21]), subsequent hourly images must be studied to see their movement. The footprint dimensions of individual pixels (the projection of a square image pixel on the ground) give the theoretical accuracy of the images, which is close to rectangular (with the alongshore side being larger). For the post-2005 data, the cross-shore footprint dimension is less than 0.2 m, while the alongshore size increases from 0.2 m at 100 m from the tower alongshore to ≈1.5 m at 400 m.

For each day in October 2011 to March 2012, the Argus image that showed the strongest signs of aeolian sand transport was selected. The aeolian transport visible on the image was then classified

according to Figure 3. A second classification used the strongest 10-min-averaged wind velocity of each day (Table 1), for which only daylight hours were used. The number of daylight hours is 11 h for October and March, 9 h for November and February, and 8 h for December and January. These hours were determined by observing the amount of light in Argus imagery.

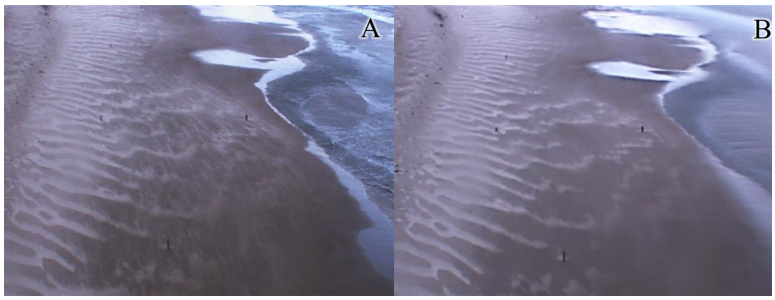

Figure 2. An example of (**A**) a snapshot image and (**B**) a timex image. Streamers are visible on the snapshot image (especially between sand strips), as a timex image blurs them out and shows the dark, moist sand instead. Sand strips, on the other hand, move so slowly that they appear almost the same in both images. The regional hourly mean wind velocity $U_{regional}$ was 8 m/s and the wind direction θ was $-97°$. Figure taken from [23].

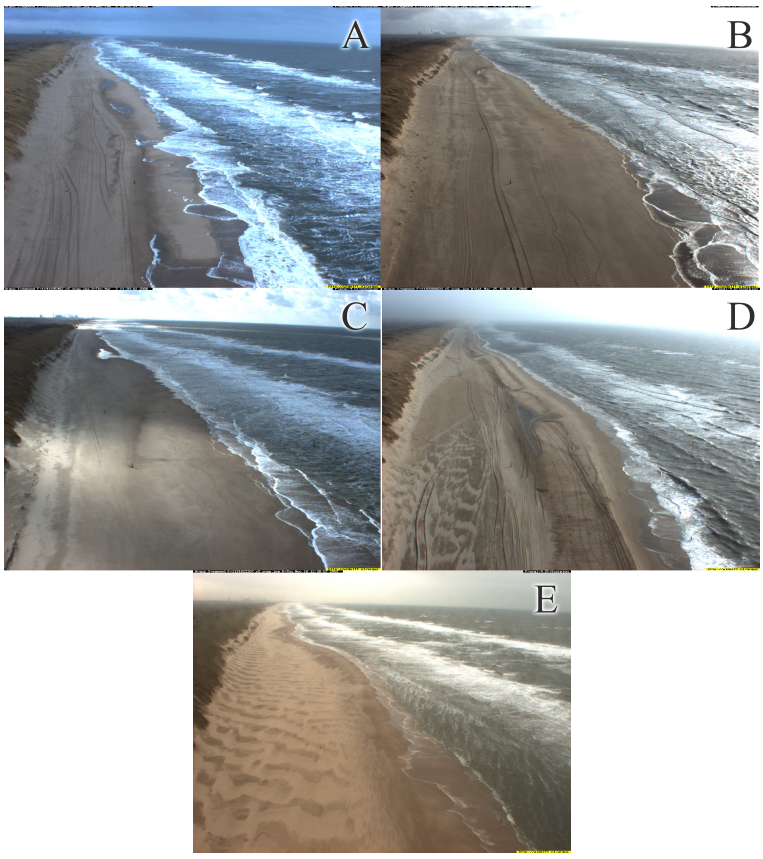

Figure 3. Snapshot images classified according to their visual signs of aeolian activity. (**A**) Class 0 shows no signs of transport; (**B**) class 1 shows very small signs of transport, like single moving patches of sand or a handful of streamers; (**C**) class 2 has more of these sand patches, but they have not formed rows of sand strips; (**D**) class 3 does have rows of sand strips, but the area they cover is patchy; and (**E**) class 4 features sand strips that cover most of the beach, often in combination with strong streamer activity. The date of the image and wind conditions were: (**A**) 08-02-2006, $U = 7$ m/s, $\theta = 23°$; (**B**) 05-03-2006, $U = 8$ m/s, $\theta = 23°$; (**C**) 02-03-2006, $U = 9$ m/s, $\theta = -17°$; (**D**) 25-03-2006, $U = 10$ m/s, $\theta = -47°$; (**E**) 10-11-2005, $U = 12$ m/s, $\theta = -57°$. Taken from [23].

Please note that the time intervals with the largest visual transport intensity is not necessarily the same as the moment with the largest wind speed. Additionally, wind directions (θ) are reported relative to shore normal in this paper, where $\theta = 0^\circ$ is cross-shore and $\theta = 90^\circ$ (-90°) alongshore from the north (south). The wind data were measured by the Royal Netherlands Meteorological Institute (KNMI) in IJmuiden, roughly 15 km south of the field site (Figure 1).

Table 1. Wind classes. The classification is based on the strongest hourly mean wind velocity measured regionally during daylight hours.

Wind Class	Wind Velocity (m/s)
1	<8.5
2	8.5–10.5
3	10.5–13.5
4	≥13.5

2.3. Model Set-Up

The model has been set up to fit the conditions found at Egmond aan Zee (Table 2). The chosen hydraulic conductivity K and infiltration coefficient C_l were obtained by minimizing the error between modelled groundwater values and observations at 5 cross-shore locations collected at the study site in October and November 2017 [49,50]. The settings for the Van Genuchten curve are taken from [34] and are also based on Egmond observations. The applied cross-shore profile is given in Figure 4. It is nearly planar with a 1:55 slope. The bed profile was made by averaging three beach profiles that crossed or were near the study site. The profiles were taken from the JARKUS dataset, annual bathymetrical and topographical measurements that provide cross-shore beach profiles along the entire Dutch coast at an interval of 200 to 250 m. For this study, the profiles closest to our study site (# 41.250, 41.500, and 41.750) measured in January 2012 have been used. The resulting alongshore-averaged bed profile, which runs from -3 m to almost +4 m with respect to MSL, was smoothed to create a monotonically increasing profile. The smoothed profile was extended with z = 4 m for another ≈150 m, where we expect oscillations in η to have dampened completely. Finally, offshore wave heights and periods, as well as water levels were measured near the harbor of IJmuiden at ten-minute intervals. The wave conditions were used to compute wave set-up and the run-up location x_{ru} in Equation (2).

The regional wind velocity U are available with a 10-min resolution. The anemometer sits at a height of 10 m above ground level. The wind must surpass a certain threshold to start sand entrainment. This was found to be ≈8 m/s for the study site, based on visual observations [21]. However, this study used regional wind data, and according to a field campaign at the study site in 2017, the local wind (i.e., on the beach) is often weaker than the regional one because of the presence of the high foredune with a steep seaward side. Refs. [13,51] illustrated with detailed wind measurements at the study site that the regional (IJmuiden) wind speed generally overestimates local wind speed, especially when the wind is blowing onshore. Here, we adapt the wind direction (θ) dependent correction factors proposed by [51] to translate regional into local wind speeds and use these local wind speeds to calculate the critical fetch and the potential transport. The ratio of regional to local wind is smallest at ≈0.60 for onshore winds and increases to ≈1 for alongshore wind (Figure 5). The data also showed that the airflow over local topography could lead to differences between regional and local wind directions close to the dune toe, as was also found by [52]. This difference is almost non-existent for the wind direction on the beach at this site. However, it has been observed that sand strips on the beach (especially when close to the dunes) can migrate in a different direction than the regional wind under almost alongshore to oblique winds [23], which indicates some wind deflection and steering.

Table 2. Used settings for the Aeolus model to represent the Egmond beach.

Spatial and temporal settings	
Start (dd-mm-yyyy)	01-10-2011
End (dd-mm-yyyy)	31-03-2012
Model output time step Δt	10 min
Spatial grid size Δx	0.5 m
Groundwater settings	
Calculation time step Δt_{gw}	2 s
Grid size	0.5 m
Aquifer depth D	11 m
Hydraulic conductivity K	4.63×10^{-4} m/s
Effective porosity n_e	0.3
Infiltration coefficient C_l	0.5
Minimum water table depth in run-up infiltration	0.2 m
Settings Van Genuchten curve	
Saturated water content w_{sat}	20.51 %
Residual water content w_{res}	2.92 %
α	5.59 m^{-1}
n	3.69
Aeolian transport settings	
α_{Hsu}	4
Grain size D_{50}	240×10^{-6} m
Maximum surface moisture content $w_{s,max}$	10%
Dunefoot elevation z_{up}	2.5 m
Minimum regional wind speed at which transport is possible U_{min}	8 m/s

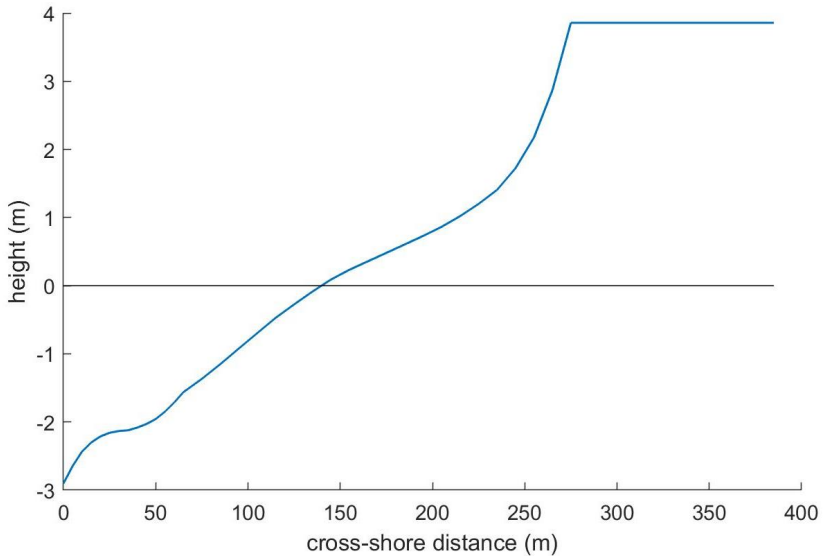

Figure 4. Smoothed Jarkus profile.

The fetch model of Aeolus can only be run for aeolian transport towards the foredune, meaning that any aeolian transport in the alongshore or offshore directions are set to zero. Sand transport with offshore winds is rare at Egmond aan Zee, and when it happens, only small visual amounts of aeolian transport are visible [23]. (Nearly) alongshore winds with a slight offshore direction, however, are responsible for the strongest visual signs of aeolian transport [23,52]. Therefore, alongshore winds between (-)90° and (-)100° (with 0° being cross-shore) were set to (-)90° to include these alongshore winds in the calculations. This filter was not applied to the Argus imagery, as we were interested in the

occurrence of sand transport under offshore winds and, therefore, when the wind direction is limiting the model. The cosine effect [3,36,53] is not included, as the focus of this study is on the timing of days with aeolian transport, not the amount of sand that will be deposited at the dune foot. The dune foot elevation z_{up} was set to 2.5 m, which is based on the beach profile at Egmond aan Zee (Figure 4). This is a little larger than the 2% exceedance value of the wave run-up maxima at the field site, which is 2.23 m in the studied period.

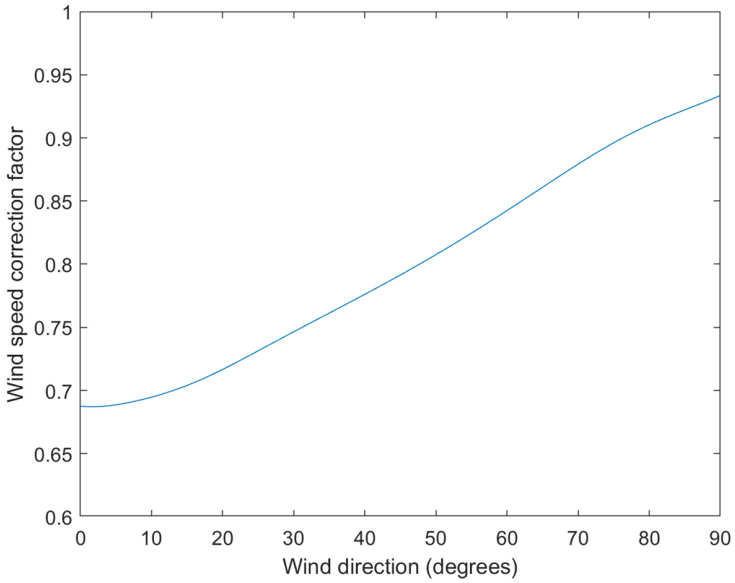

Figure 5. The correction factor needed when computing the local from regional wind velocities as a direction of regional wind direction. 0° is cross-shore (onshore).

2.4. Synthetic Runs

Several synthetic simulations were run to illustrate the output of the model and to aid in the interpretation of the Egmond simulations. We focus here on moisture and, in particular, aeolian transport rates, as output from the groundwater model have already been discussed extensively in [30,34]. The imposed conditions were a semi-diurnal tide of 12 h and 25 min with an amplitude of 1.5 m and a wave period and height of 5 s and 1.2 m, respectively. The regional wind direction θ varied from 0° to ±90° (with 0° being onshore) with a 15° step size and the regional wind speed was varied from 8 to 23 m/s with intervals of 5 m/s for each direction. To mimic the Egmond situation, the regional wind speed was transformed to the local wind. All other variables and parameters were set to fit the Egmond site (see Section 2.3). Each simulation was run for 30 days to account for the model's spin up time. The results below focus on the 30th day.

Figure 6 shows the output of the surface moisture model. The upper part of the intertidal zone (between 220 and 240 m) slowly dries during low tide, and inundates quickly with rising tide. Please note that most of the intertidal beach remains too wet to sustain aeolian transport (w_s >10%). Figure 7 shows nine examples of the synthetic runs, displaying the actual transport rate q_a at z_{up} = 2.5 m (at $x \approx$ 260 m in Figure 6), the potential transport rate q_p based on [1], and the imposed offshore tide. Obviously, q_p does not depend on time, but because of the imposed wind speed correction it does depend on θ. In contrast, q_a can vary with time, as it does, for example, when θ = 15° and $U_{regional}$ = 18 or 23 m/s (Figure 7A). The largest values for q_a were not reached at low tide when the beach is at its widest, but approximately 2 h before high tide, when the surface moisture at the upper intertidal zone is smallest, hence providing the largest surface of dry sand (Figure 6). The groundwater level keeps on falling until the beach is inundated by the tide. The groundwater level and surface moisture content at high tide (time = 3:21 h in Figure 7) and low tide (time = 9:36 h in Figure 7) are shown in Figure 8A

and B, respectively. The groundwater level is close to the bed for most parts of the intertidal beach during the tidal cycle and the surface moisture always keeps its maximum value, w_{sat}. Only around x= 240 m, the surface moisture drops below 10% to allow aeolian transport during certain parts of the tide. Qualitatively, this is consistent with suggestions in [30,54] that the contribution of the intertidal zone as a sand source for aeolian transport is limited.

In general, q_a is less than q_p for θ = 15°, except for the smallest wind velocity $U_{regional}$ = 13 m/s. Then, q_a is smaller than q_p during high tide only (Figure 7A). The larger the wind velocity, the larger the difference between q_a and q_p. Similar results can also be seen for θ = 45° (Figure 7B), but not when θ = 75° (Figure 7C). Now, $q_a = q_p$ in all simulations. This (lack of) difference between q_a and q_p is further illustrated in Figure 9. Both q_a and q_p, averaged for a single tide, increase when the wind becomes more alongshore, and the wind speed increases. For q_p (Figure 9A), the difference with θ is caused by the wind speed correction while for q_a, θ also affects the maximum fetch. When the angle of the wind is almost alongshore, the critical fetch length F_c is reached and exceeded even at high tide, which causes q_a and q_p to be the same. Little to no potential and actual transport can be expected for small wind velocities no matter the direction. Figure 9C shows the standard deviation in q_a. A zero standard deviation implies q_a does not vary with the tide. This happens when the wind is (almost) alongshore. The critical fetch is then reached during the entire tidal cycle. With oblique winds, the maximum fetch length varies greatly, allowing the critical fetch to be (almost) reached only during low tide. This results in the largest standard deviations. With cross-shore winds, the maximum fetch length still varies, but it will do so less than for oblique winds, and, consequently, the standard deviation reduces again.

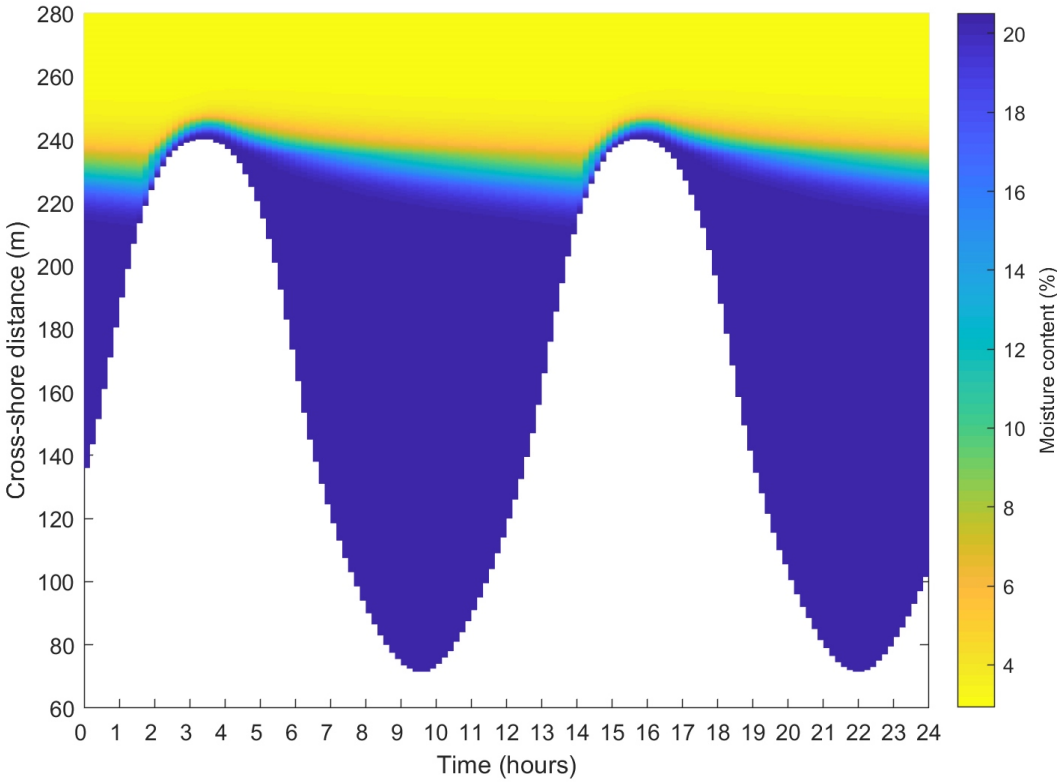

Figure 6. Surface moisture model output for a 12.5 h tide with an amplitude of 1.5 m, a wave height of 1.2 m, a wave period of 5 s, and using the parameters and bed profile for Egmond aan Zee. The figure depicts the model output for day 30 of the studied time period. The cross-shore distance runs from the sea (**bottom** of the figure) to the dunes (**top** of figure).

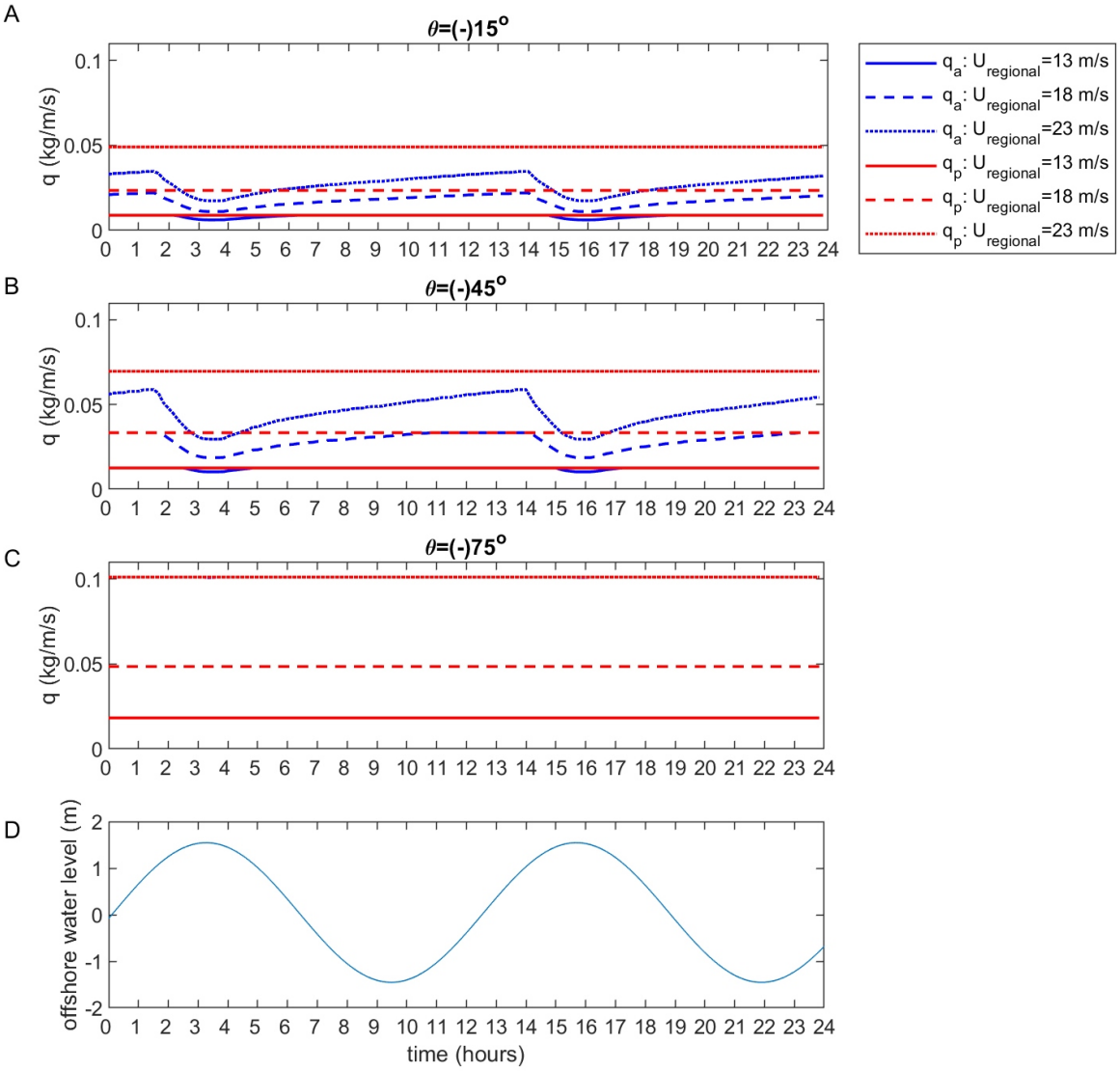

Figure 7. Aeolian transport rate q_a as calculated by Aeolus and the potential transport rate q_p based on wind velocity alone at $x \approx 260$ m ($z_{up} = 2.5$ m) for (**A**) $\theta = 15°$, (**B**) $\theta = 45°$, and (**C**) $\theta = 75°$. This transport does not take the cosine effect into account. (**D**) shows the tide for reference.

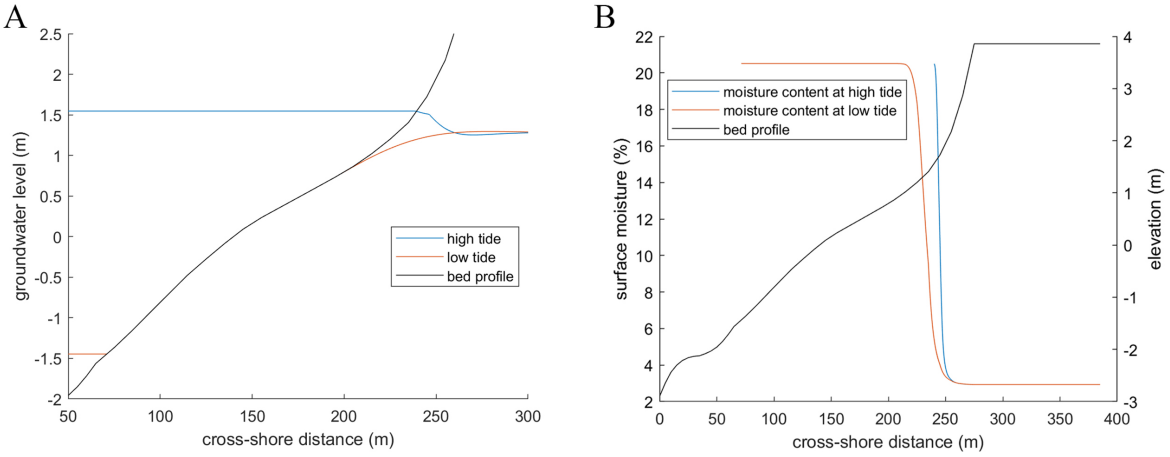

Figure 8. (**A**) Groundwater level during high and low tide and (**B**) surface moisture during high and low tide modelled by Aeolus.

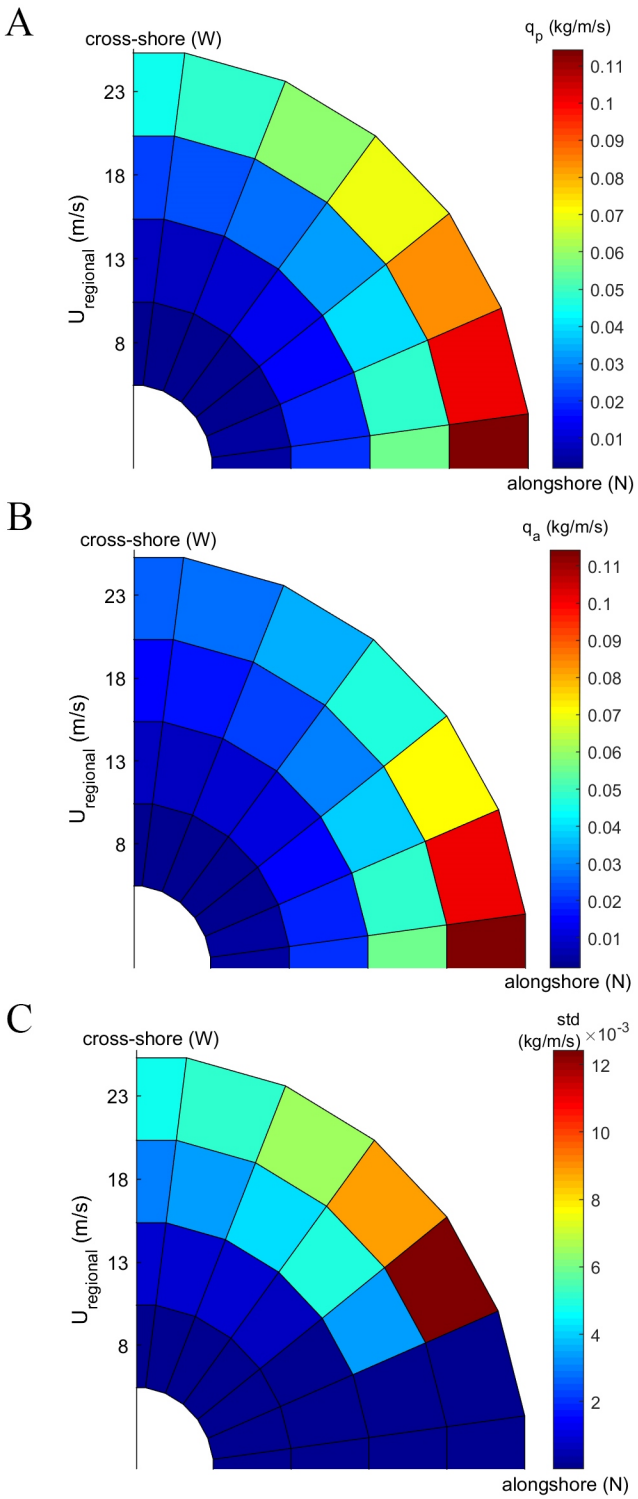

Figure 9. (**A**) Mean potential aeolian transport rate q_p for various wind velocities and directions, (**B**) mean actual aeolian transport rate q_a, and (**C**) the standard deviation in q_a, calculated for a single tide and various wind velocities and directions. There are 4 values for the regional wind velocity, which increase from inner to outer ring, and 7 different wind directions.

3. Results

The most common regional wind speed during the studied time period from October 2011 to March 2012 was around 5 m/s (Figure 10A), while the average regional wind speed was 6.6 m/s.

The largest wind speed encountered was 24 m/s. The dominant wind direction was south-west, followed by nearly westerly winds (Figure 10B). Westerly winds also showed a relatively large percentage of strong winds (>13.5 m/s).

Table 3 displays the number of days with transport sorted according to their largest 10-min-averaged wind velocity measured during daylight hours and their strongest visual signs of transport. A few days (November 10, 17, and 21) could not be studied as fog obscured the beach during the entire day. Most of the 183 days show either no (class 0, 126 days) or substantial visual signs (class 4, 28 days) of aeolian transport. According to [23], strong winds but no or limited transport indicate supply-limited conditions at the beach. How large the wind speed has to be for limited transport depends on the strength of the visual aeolian transport; a transport day with no visual sign of transport is considered limited when the wind speed is above the threshold of transport (≈8 m/s for Egmond aan Zee). The wind speed must be larger when stronger visual signs are present. That means that all days of visual transport class 0 in Table 3, many of visual transport class 1, and some of visual transport class 2 and 3 are probably limited.

Table 3. Days sorted according to their wind class (Table 1) and visual transport class (Figure 3), with the total number of days for each class and the corresponding percentage.

	Visual Transport Class						
Wind Class	0	1	2	3	4	Total	Percentage
1	84	1	1	1	0	87	47.5%
2	20	4	4	1	10	39	21.3%
3	15	5	1	3	5	29	15.8%
4	7	4	1	3	13	28	15.3%
Total	126	14	7	8	28	183	
Percentage	68.8%	7.7%	3.8%	4.4%	15.3%		

Figure 11A shows the hourly average predicted potential and actual transport during daylight hours, together with the strongest visual classification of Argus imagery of the corresponding day. The corresponding wind direction and velocity is shown in Figure 11B. Visual signs of aeolian transport were especially common in the end of November and in December 2011, during which the wind was relatively strong. March 2012, in contrast, had weak winds and contained only a few Argus images with visual transport. Offshore winds usually do not create aeolian bedform, which was the case for most days in November. This corresponds qualitatively with the model predictions, which are largest during the second half of November and December. The day with the largest average predicted potential and predicted actual transport is 3 January 2012, reaching 265.4 and 251.2 kg/m/h, respectively. The intensity of the visual signs of aeolian transport on the Argus images generally corresponds with the amount of predicted actual transport, with a stronger visual class generally having a larger predicted actual transport. There are, however, several days (e.g., October 5, 6, 7, and 12, 2011), for which q_a was predicted to be relatively large (≈50 kg/m/h, which was almost the same as q_a on those days), but Argus showed minimal signs of aeolian activity (class 1). The other way around, with small q_a (≈10 kg/m/h), but strong visual signs of transport (class 4), happened occasionally too (e.g., October 21, 26, and 30).

On 30 of the total 183 days the model predictions and Argus observations did not agree in the sense that Argus showed no transport but q_a was non-zero. These mismatches tend to occur on days with little transport, as on 27 days the potential transport was less than 10% of the maximum predicted potential transport. This may imply that small transport rates are not well visible, and are thus incorrectly classified as transport class 0. On 5 days, visual signs of transport were present, but the model predicted zero q_a. These mismatches will be examined further in the Discussion section of this paper.

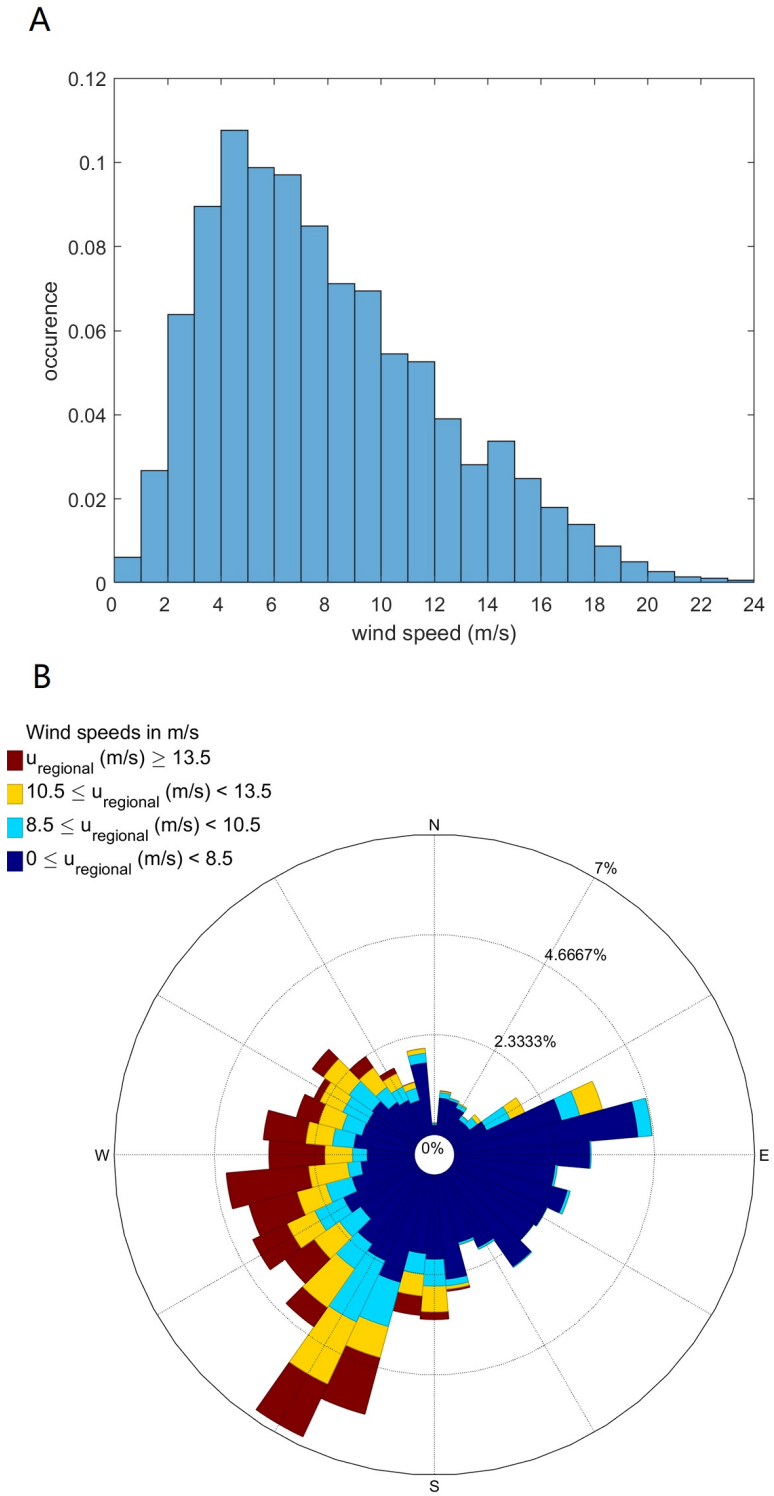

Figure 10. (**A**) Histogram of the wind speed and (**B**) a windrose showing the direction and speed of the wind at the KNMI weather station in IJmuiden from October 2011 to March 2012. The coastline has an approximate north-south orientation.

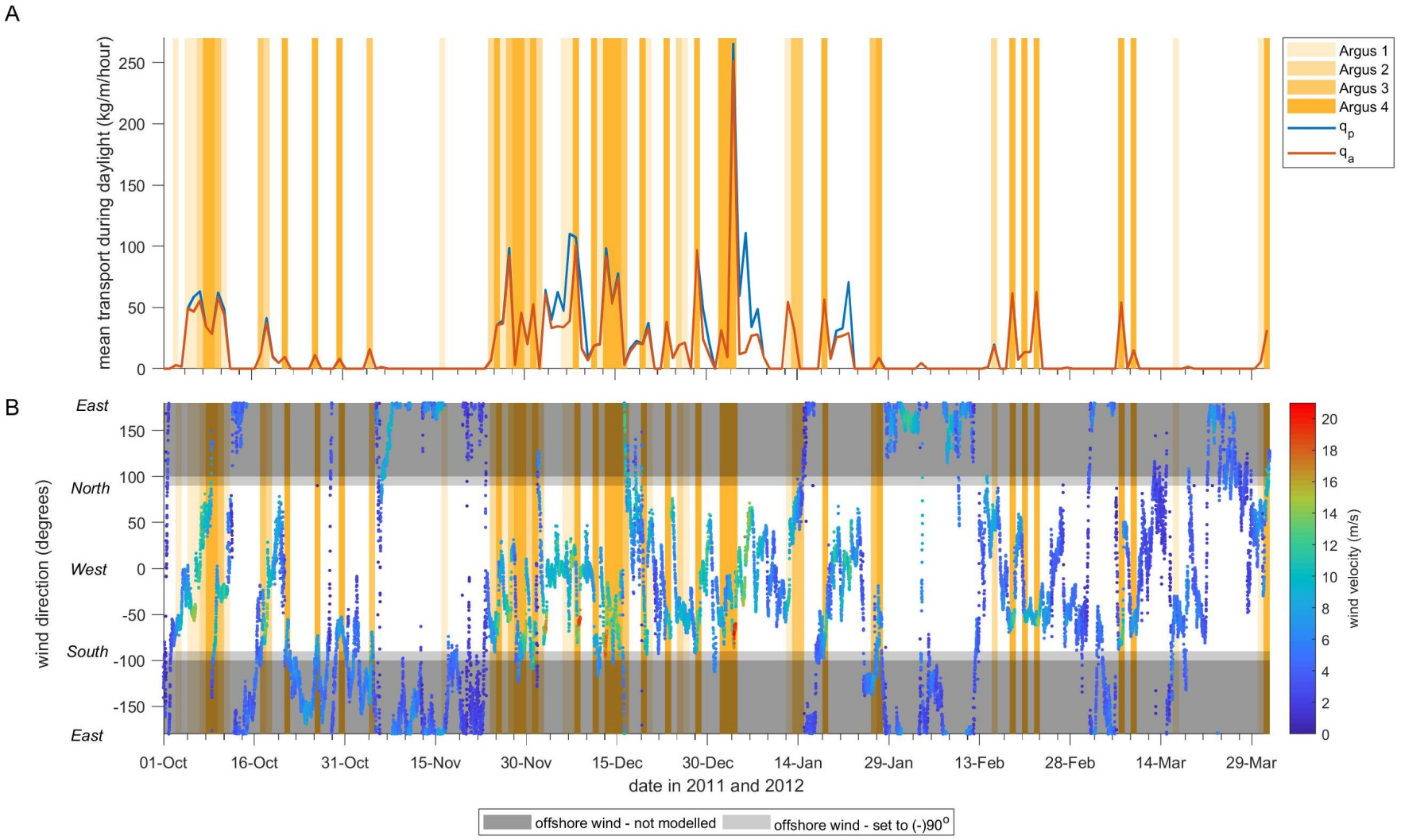

Figure 11. (**A**) Time series of predicted hourly average potential and actual transport (daylight hours only) and the strongest observed visual transport for each day. (**B**) the corresponding wind direction and velocity. Aeolus cannot model offshore wind. Winds that were offshore, but nearly alongshore (with θ between (-)90° and (-)100°) were set to $\theta =$ (-)90°.

Figure 11A illustrates that q_a was often predicted to be regularly smaller than q_p, in other words, that transport at the dune line is limited. Table 4 provides the average ratio of q_a and q_p for each visual class (using daily sums of daylight hours only for all cases with non-zero q_p). Several days, but especially in visual transport class 0 (97 out of 126), result in $q_p = q_a = 0$. This is caused by offshore winds filtered out by Aeolus, except for wind class 1; here, the non-zero values are almost all caused by a wind speed smaller than the threshold of motion (40 of these days showed a combination of a small wind speed and an offshore wind). Two days with offshore wind form an exception. Even though the wind speed on these days surpassed the threshold of motion, it did not cause any visual signs of aeolian transport (visual transport class 0).

The q_a to q_p ratios are (close to) 1 for most wind and visual transport classes. The smallest ratios for q_a/q_p can be found in strong wind classes (class 3 and 4) with little visual transport (class 0 and 1). Some classes contain only a few days, which makes it hard to draw conclusions, but the general trend of small q_a/q_p for strong wind classes (class 3 and 4) in combination with small visual transport classes (class 0 and 1) corresponds to the expectation of limited transports for these conditions. Also, $q_a/q_p \approx 1$ otherwise is consistent with expectations. Strong winds with little visible transport seem to be fetch limited, or were classified as having no visual transport because the aeolian transport is too small to be visible on the imagery. It was found in [23] that weak winds could still cause a large amount of aeolian bedforms, but probably only when there is sufficient time to develop them.

Table 4. Mean q_a/q_p for the days from Table 3. When there is no number, there either are no days that fall within this wind and visual transport class or q_a and q_p are zero. The numbers between parentheses show the number of days where q_a and q_p are non-zero and the total number of days in that class.

	Visual Transport Class				
Wind Class	0	1	2	3	4
1	1.00 (2 out of 84)	- (0 out of 1)	- (0 out of 1)	- (0 out of 1)	- (0 out of 0)
2	0.94 (11 out of 20)	0.99 (3 out of 4)	0.98 (4 out of 4)	- (0 out of 1)	1.00 (10 out of 10)
3	0.77 (10 out of 15)	0.91 (5 out of 5)	0.91 (1 out of 1)	0.98 (3 out of 3)	1.00 (5 out of 5)
4	0.46 (6 out of 7)	0.76 (4 out of 4)	0.88 (1 out of 1)	0.98 (3 out of 3)	0.98 (13 out of 13)

The ratio of q_a/q_p depends on the wind speed and direction. The wind rose in Figure 12A is based on wind data with $q_a/q_p < 0.8$ and in Figure 12B with $q_a/q_p \geq 0.8$. When q_a/q_p <0.80, the wind is mostly strong and predominantly onshore directed. This wind direction is the most common for visual transport class 0 with wind class 3 and 4. Alongshore winds, on the other hand, are almost completely absent in this wind rose. The situation with $q_a/q_p \geq$0.80 corresponds to winds with a predominantly alongshore direction. The few days when the wind blew onshore (from the west), the wind velocity generally did not exceed 12 m/s. Relatively small wind velocities (<9.5 m) are more common here than in Figure 12A. These findings are largely consistent with the results from the synthetic runs. It also corresponds to [23], who found that the wind direction is important during large wind speeds; only under alongshore winds the fetch length will be long enough for unlimited transport.

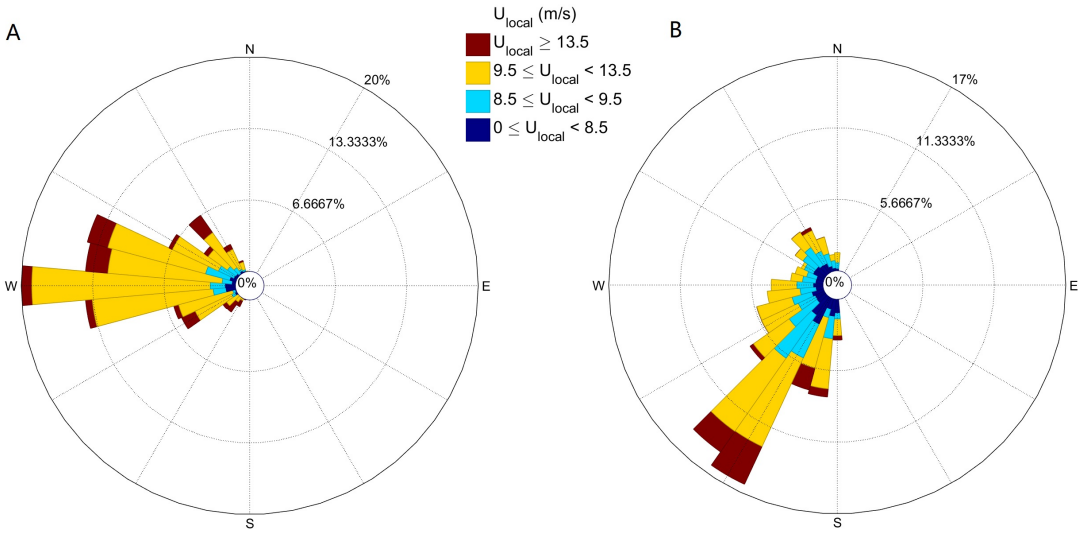

Figure 12. (**A**) Wind rose consisting of transport days when q_a/q_p <0.80 and (**B**) when q_a/q_p ≥0.80.

4. Discussion

4.1. Model Performance

The dataset from October 2011 to March 2012 of the Argus video monitoring station at Egmond aan Zee was classified according to their visual signs of aeolian transport days. Their timing and class were compared with the aeolian transport rates predicted by the Aeolus model. The visual signs of aeolian transport on the Argus images coincided well with Aeolus for most days (148 out of 183). The model gave limited transport rates (i.e., when q_a/q_p is <0.80 in this research) for winds with a predominantly cross-shore direction and larger wind velocities (≥13 m/s). This is qualitatively consistent with other narrow beach studies [3,5].

On 30 days Aeolus predicted non-zero transport rates while no transport was visible on the Argus imagery. For most (27) of these days, average transport rates were predicted to be small (<25 kg/m/h using daylight hours only), and it is possible that these small rates leave no visual signature on the Argus imagery. Five of the 27 days showed signs of rain or snow, or had very low temperatures (presumably causing a frozen beach), which may have prevented aeolian transport. The Aeolus model does not incorporate these limiting factors. The present results suggest it may be worthwile to include these meteorological variables to filter out the days of zero transport, in a similar fashion as in [25].

There were 3 periods in the dataset when Argus imagery showed no sign of aeolian transport while Aeolus predicted relatively strong transport rates (≥25 kg/m/h). In all these cases, the Argus images were difficult to interpret, and it is thus possible that these classes 0 were incorrectly classified as such. On the first of these periods, December 3 to 5, 2011, the imagery showed contrast between dark, wet sand, and light, dry sand that grew in area. This was interpreted as drying of the sand, and therefore a visual transport class 0, but it could have been caused by transported sand too. Furthermore, it was raining, which might have hindered the development of sand strips. The second period, January 6 and 7, 2012, might have signs of transport next to a small scarp in the dunefront, but again, the Argus images were difficult to interpret. The third period, January 20 to 22, 2012, suffers from Argus images taken under relatively bad light conditions, which makes it hard to discern small traces of transport.

Five days showed visual transport while the Aeolus model predicted zero q_a. For two of these days, 2 December 2012, and 16 March 2012, the Argus imagery might have been classified incorrectly as their interpretation was difficult. The situation on 16 November 2011 was classified as visual transport class 1, showing only a few visual traces of aeolian transport. Overall, we do not consider this mismatch to be a large error, as the difference between no and little transport here is small. The images of 14

January 2012 on the other hand, showed a medium strong visual sign of transport (class 3), even though the wind velocity did not exceed the threshold of motion. The period of visual aeolian transport lasted no more than an hour. The wind causing it might have been too local to be registered by the weather station in IJmuiden, and therefore resulted in a q_a of zero. Also, wind gusts above the threshold may have caused some transport, but gustiness is not included in Aeolus. The images of 26 January 2012 showed strong signs of transport (class 4). The wind direction was larger than 100° for most of the day, meaning its transport rate was set to zero by Aeolus. On this day, the days when the wind direction was less than 100°, the wind velocity was below the threshold of motion. This case shows that the threshold of 100° might not have been large enough to include all days that cause alongshore aeolian transport. Offshore winds that have a more cross-shore direction usually do not cause visible signs of aeolian transport at the Egmond study site, which makes Aeolus work reasonably well for this site. This might not be the case for other beaches, where studying and modelling aeolian transport events by offshore events, as was done by [55,56], is far more essential. Overall, most Argus-Aeolus mismatches are thus induced by poor classification of Argus imagery, where the visual signs of aeolian transport are too small to be observed properly. For a few cases, precipitation and frost could be the cause of a mismatch. Exceeding the wind direction threshold was the cause of a mismatch for one day.

Finally, we note that the days with strong signs of aeolian transport did not always coincide with large predicted transport rates (Figure 11). Underdeveloped or no sand strips (class 0, 1, and 2), however, do seem to be more common when q_a differs strongly from q_p, which can be seen for October 5 and 6, December 5 to 7, January 4 to 7, and January 20 to 22. The development of sand strips might be hindered by a moist surface or a short fetch during these days, meaning that well-developed signs of aeolian transport are more likely to appear on days with unhindered sand transport, not necessarily on days with large potential transport rates.

4.2. Relevance of Days with Limited Transport

Although, as indicated in Table 4, the ratio of q_a to q_p is often large, the days when q_a is well below q_p do have a large influence on the cumulative transport in the study period. This is further illustrated with Figure 13. The total q_p and q_a from October 2011 to March 2012 (including night hours) is 6.6×10^4 kg/m and 5.2×10^4 kg/m, respectively. The amount of sand that reaches the dune foot (implementing the cosine effect) is 3.7×10^4 kg/m and 2.7×10^4 kg/m for q_p and q_a, respectively. This amount is larger than observed (see also [13]), as the dune volume at this site increases with 2.3×10^4 kg/m/year during accretion periods [57]. An interesting future step is to calculate aeolian transport rates in supply-limited conditions, like the AeoLis model developed by [58].

Both q_a and q_p follow a comparable cumulative trend, but their difference does not increase gradually with time. Instead, only a few individual days seem to invoke sudden, substantial differences (e.g., 5 to 9 December 2011 and 3 January 2012). It is interesting to note that only parts of these days had limited transport. During the days in December, the wind was strong (>11 m/s) and fluctuated in direction. When it was (close to) cross-shore, it caused limited transport. January 3 started with very strong winds of ≈20 m/s. Since these winds were shore-oblique, the fetch length was close to the critical fetch length, causing q_a/q_p to fluctuate between 1.00 (low tide) and 0.80 (high tide). Only when the wind changed to a more cross-shore direction at the end of the day, q_a/q_p dropped to 0.45. This further stresses that the limitation in only a few days with large potential transport may have a profound effect on long-term aeolian transport. Future work is needed to test the generality of this finding, including in-depth analyses of these complex events and the possibility of increasing the temporal resolution of visual transport classifications from daily to hourly.

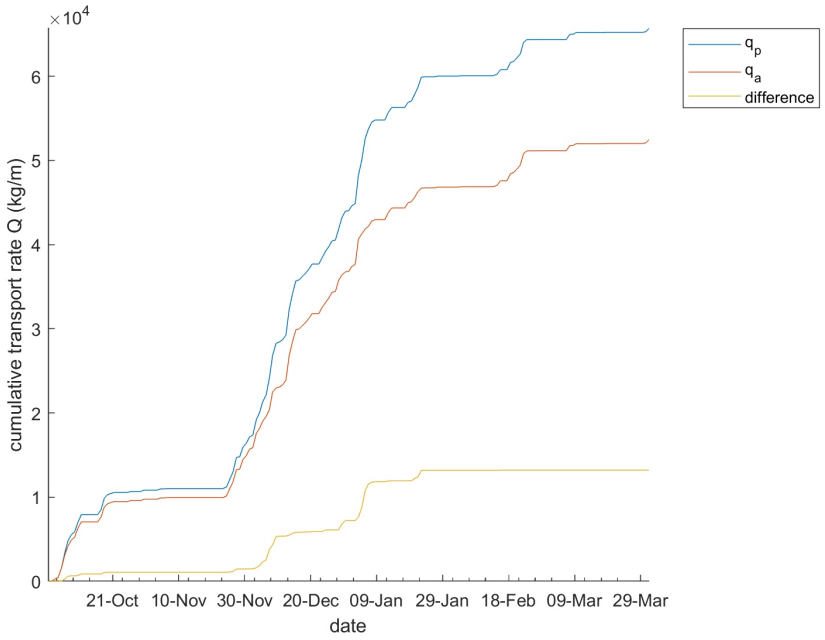

Figure 13. Cumulative sum of Q_a and Q_p, and their difference.

5. Conclusions

The Aeolus model was developed to make better predictions of aeolian sand transport rates on narrow beaches by including wind- and moisture-induced fetch effects. To test if the model predicts the timing and transport-limited nature of aeolian transport events correctly, its results were compared to Argus images collected during a six-month winter period at Egmond aan Zee (the Netherlands). The medium to strong transport events predicted by Aeolus usually coincided with strong visual signs of aeolian transport in the images. Consistent with visual signs of limited transport, Aeolus sometimes predicted the actual transport to be smaller than the potential transport. Strong differences are more common for strong and onshore winds. Furthermore, it was observed that strong visual signs of aeolian transport overlapped with either equal actual and potential transport (i.e., no limitation), or when the actual transport was relatively large. Mismatched days usually had no visual sign of aeolian transport on the corresponding Argus images and only small transport rates predicted by Aeolus. It is possible that these aeolian transports are too small to be seen on Argus, or that a limiting factor not taken into account by Aeolus, like rain or snow, was enough to end this small amount of aeolian transport. This semi-quantitative research shows that overall, the Aeolus model predicts the timing of sand transport well for a long, multiple-month time period.

Author Contributions: conceptualization, P.H. and G.R.; methodology, P.H., G.R.; software, P.H., G.R., Z.v.A.; validation, P.H., G.R. and J.D.; formal analysis, P.H.; investigation, P.H., Z.v.A.; resources, G.R.; data curation, P.H.; writing—original draft preparation, P.H.; writing—review and editing, G.R. and J.D.; visualization, P.H.; supervision, G.R. and J.D.; project administration, G.R.; funding acquisition, G.R. All authors have read and agreed to the published version of the manuscript.

Funding: This study was funded by the Dutch Technology Foundation STW (Vici project 13709), which is part of the Netherlands Organisation for Scientific Research (NWO), and which is partly funded by the Ministry of Economic Affairs.

Acknowledgments: We wish to thank Bas van Dam, the late Irv Elshoff, John Stanley and Rob Holman for Argus support. We also want to thank Irene Delgado-Fernandez and Bernard Bauer for their extensive feedback.

Conflicts of Interest: The authors declare no conflict of interest. The funders had no role in the design of the study; in the collection, analyses, or interpretation of data; in the writing of the manuscript, or in the decision to publish the results.

References

1. Hsu, S.A. Computing Eolian Sand Transport from Routine Weather Data. *Coast. Eng.* **1974**, 1619–1626. [CrossRef]
2. Davidson-Arnott, R.G.D.; Law, M.N. Measurement and prediction of long-term sediment supply to coastal foredunes. *J. Coast. Res.* **1996**, *12*, 654–663.
3. Bauer, B.O.; Davidson-Arnott, R.G.D. A general framework for modeling sediment supply to coastal dunes including wind angle, beach geometry, and fetch effects. *Geomorphology* **2002**, *49*, 89–108. [CrossRef]
4. Sherman, D.J.; Houser, C.; Baas, A.C.W. *Electronic Measurement Techniques for Field Experiments in Process Geomorphology*; Elsevier Ltd.: New York, NY, USA, 2013; Volume 14, pp. 195–221. [CrossRef]
5. Delgado-Fernandez, I.; Davidson-Arnott, R.G.D. Meso-scale aeolian sediment input to coastal dunes: The nature of aeolian transport events. *Geomorphology* **2011**, *126*, 217–232. [CrossRef]
6. Edwards, B.L.; Namikas, S.L. Small-scale variability in surface moisture on a fine-grained beach: implications for modeling aeolian transport. *Earth Surf. Process. Landf.* **2009**, *34*, 1333–1338. [CrossRef]
7. Wiggs, G.F.S.; Atherton, R.J.; Baird, A.J. Thresholds of aeolian sand transport: establishing suitable values. *Sedimentology* **2004**, *51*, 95–108. [CrossRef]
8. Nield, J.M.; King, J.; Wiggs, G.F.S.; Leyland, J.; Bryant, R.G.; Chiverrell, R.C.; Darby, S.E.; Eckardt, F.D.; Thomas, D.S.G.; Vircavs, L.H.; et al. Estimating aerodynamic roughness over complex surface terrain. *J. Geophys. Res. Atmos.* **2013**, *118*, 12948–12961. [CrossRef]
9. Nield, J.M.; King, J.; Jacobs, B. Detecting surface moisture in aeolian environments using terrestrial laser scanning. *Aeolian Res.* **2014**, *12*, 9–17. [CrossRef]
10. Svasek, J.N.; Terwindt, J.H.J. Measurements of sand transport by wind on a natural beach. *Sedimentology* **1974**, *21*, 311–322. [CrossRef]
11. Jackson, N.L.; Nordstrom, K.F. Aeolian transport of sediment on a beach during and after rainfall, Wildwood, NJ, USA. *Geomorphology* **1998**, *22*, 151–157. [CrossRef]
12. Sherman, D.J.; Jackson, D.W.; Namikas, S.L.; Wang, J. Wind-blown sand on beaches: An evaluation of models. *Geomorphology* **1998**, *22*, 113–133. [CrossRef]
13. de Winter, W.; Donker, J.; Sterk, G.; Van Beem, J.; Ruessink, G. Regional versus local wind speed and direction at a narrow beach with a high and steep foredune. *PLoS ONE* **2020**, *15*. [CrossRef] [PubMed]
14. Bauer, B.O.; Davidson-Arnott, R.G.; Nordstrom, K.F.; Ollerhead, J.; Jackson, N.L. Indeterminacy in aeolian sediment transport across beaches. *J. Coast. Res.* **1996**, *12*, 641–653.
15. Bauer, B.O.; Davidson-Arnott, R.G.D.; Hesp, P.A.; Namikas, S.L.; Ollerhead, J.; Walker, I.J. Aeolian sediment transport on a beach: Surface moisture, wind fetch, and mean transport. *Geomorphology* **2009**, *105*, 106–116. [CrossRef]
16. Baas, A.C.W.; Sherman, D. Formation and behavior of aeolian streamers. *J. Geophys. Res. Earth Surf.* **2005**, *110*. [CrossRef]
17. Sherman, D.J.; Li, B. Predicting aeolian sand transport rates: A reevaluation of models. *Aeolian Res.* **2012**, *3*, 371–378. [CrossRef]
18. Montreuil, A.L.; Chen, M.; Brand, E.; Strypsteen, G.; Rauwoens, P.; Vandenbulcke, A.; De Wulf, A.; Dan, S.; Verwaest, T. Dynamics of Surface Moisture Content on a Macro-tidal Beach. *J. Coast. Res.* **2018**, *85*, 206–210. [CrossRef]
19. Nield, J.M.; Wiggs, G.F.S.; Squirrell, R.S. Aeolian sand strip mobility and protodune development on a drying beach: examining surface moisture and surface roughness patterns measured by terrestrial laser scanning. *Earth Surf. Process. Landf.* **2011**, *36*, 513–522. [CrossRef]
20. Nield, J.M. Surface moisture-induced feedback in aeolian environments. *Geology* **2011**, *39*, 915–918. [CrossRef]
21. Hage, P.M.; Ruessink, B.G.; Donker, J.J.A. Determining sand strip characteristics using Argus video monitoring. *Aeolian Res.* **2018**, *33*, 1–11. [CrossRef]
22. Delgado-Fernandez, I.; Davidson-Arnott, R.G.D.; Ollerhead, J. Application of a Remote Sensing Technique to the Study of Coastal Dunes. *J. Coast. Res.* **2009**, *255*, 1160–1167. [CrossRef]
23. Hage, P.M.; Ruessink, B.G.; Donker, J.J.A. Using Argus video monitoring to determine limiting factors of aeolian sand transport on a narrow beach. *J. Mar. Sci. Eng.* **2018**, *6*, 138. [CrossRef]

24. Van der Wal, D. Effects of fetch and surface texture on aeolian sand transport on two nourished beaches. *J. Arid Environ.* **1998**, *39*, 533–547. [CrossRef]
25. Delgado-Fernandez, I. Meso-scale modelling of aeolian sediment input to coastal dunes. *Geomorphology* **2011**, *130*, 230–243. [CrossRef]
26. Raubenheimer, B.; Guza, R.; Elgar, S. Tidal water table fluctuations in a sandy ocean beach. *Water Resour. Res.* **1999**, *35*, 2313–2320. [CrossRef]
27. Nielsen, P. Tidal dynamics of the water table in beaches. *Water Resour. Res.* **1990**, *26*, 2127–2134. [CrossRef]
28. Nielsen, P.; Davis, G.; Winterbourne, J.; Elias, G. Wave setup and the watertable in sandy beaches. *Tech. Rep. Tech. Memo-Randum* **1998**, *88*, 1.
29. Kang, H.Y.; Nielsen, P.; Hanslow, D.J. Watertable overheight due to wave runup on a sandy beach. *Coast. Eng.* **1994**, 2115–2124.
30. Brakenhoff, L.B.; Smit, Y.; Donker, J.J.; Ruessink, G. Tide-induced variability in beach surface moisture: Observations and modelling. *Earth Surf. Process. Landf.* **2019**, *44*, 317–330. [CrossRef]
31. Turner, I.L.; Nielsen, P. Rapid water table fluctuations within the beach face: Implications for swash zone sediment mobility? *Coast. Eng.* **1997**, *32*, 45–59. [CrossRef]
32. Stockdon, H.F.; Holman, R.A.; Howd, P.A.; Sallenger Jr, A.H. Empirical parameterization of setup, swash, and runup. *Coast. Eng.* **2006**, *53*, 573–588. [CrossRef]
33. Huizer, S.; Karaoulis, M.; Oude Essink, G.; Bierkens, M. Monitoring and simulation of salinity changes in response to tide and storm surges in a sandy coastal aquifer system. *Water Resour. Res.* **2017**, *53*, 6487–6509. [CrossRef]
34. Smit, Y.; Donker, J.; Ruessink, B. Spatiotemporal surface moisture variations on a barred beach and their relationship with groundwater fluctuations. *Hydrology* **2019**, *6*, 8. [CrossRef]
35. Van Genuchten, M.T. A closed-form equation for predicting the hydraulic conductivity of unsaturated soils 1. *Soil Sci. Soc. Am. J.* **1980**, *44*, 892–898. [CrossRef]
36. Delgado-Fernandez, I. A review of the application of the fetch effect to modelling sand supply to coastal foredunes. *Aeolian Res.* **2010**, *2*, 61–70. [CrossRef]
37. Hsu, S.A. Wind stress criteria in eolian sand transport. *J. Geophys. Res.* **1971**, *76*, 8684–8686. [CrossRef]
38. Wijnberg, K.M.; Terwindt, J.H.J. Extracting decadal morphological behaviour from high-resolution, long-term bathymetric surveys along the Holland coast using eigenfunction analysis. *Mar. Geol.* **1995**, *126*, 301–330. [CrossRef]
39. Quartel, S.; Ruessink, B.G.; Kroon, A. Daily to seasonal cross-shore behaviour of quasi-persistent intertidal beach morphology. *Earth Surf. Process. Landf.* **2007**, *32*, 1293–1307. [CrossRef]
40. Sluijter, R.; Leenaers, H.; Camarasa, M. *De Bosatlas van het klimaat*; Noordhoff uitgevers Groningen: Groningen, The Netherlands, 2011. Available online: www.klimaatatlas.nl (accessed on 11 February 2020).
41. Masselink, G.; Kroon, A.; Davidson-Arnott, R.G.D. Morphodynamics of intertidal bars in wave-dominated coastal settings—A review. *Geomorphology* **2006**, *73*, 33–49. [CrossRef]
42. Aagaard, T.; Kroon, A.; Andersen, S.; Sørensen, R.M.; Quartel, S.; Vinther, N. Intertidal beach change during storm conditions; Egmond, The Netherlands. *Mar. Geol.* **2005**, *218*, 65–80. [CrossRef]
43. Quartel, S.; Grasmeijer, B.T. Dynamiek van het strand bij Noordwijk aan Zee en Egmond aan Zee en het effect van suppleties. In *Rijksinstituut voor Kust en Zee (RIKZ)*; Opdracht RKZ-1667; Universiteit van Utrecht: Utrecht, The Netherlands, 2007.
44. de Winter, R.C.; Gongriep, F.; Ruessink, B.G. Observations and modeling of alongshore variability in dune erosion at Egmond aan Zee, the Netherlands. *Coast. Eng.* **2015**, *99*, 167–175. [CrossRef]
45. Ruessink, B.; Schwarz, C.; Price, T.; Donker, J. A Multi-Year Data Set of Beach-Foredune Topography and Environmental Forcing Conditions at Egmond aan Zee, The Netherlands. *Data* **2019**, *4*, 73. [CrossRef]
46. van Enckevort, I.M.J.; Ruessink, B.G. Effect of hydrodynamics and bathymetry on video estimates of nearshore sandbar position. *J. Geophys. Res. Oceans* **2001**, *106*, 16969–16979. [CrossRef]
47. Holman, R.A.; Sallenger, A.H. High-energy nearshore processes. *Eos Trans. Am. Geophys. Union* **1986**, *67*, 1369. [CrossRef]
48. Holman, R.A.; Stanley, J. The history and technical capabilities of Argus. *Coast. Eng.* **2007**, *54*, 477–491. [CrossRef]
49. Tuijnman, Y. *Soil Moisture Dynamics and the Effects on Initiation of Aeolian Sand Transport*; Utrecht University: Utrecht, The Netherlands, 2019.

50. Smit, Y. Surface Moisture Dynamics on a Narrow Coastal Beach. Ph.D. Thesis, Utrecht University, Utrecht, The Netherlands, 2019.
51. Ruessink, G.; Schwarz, C.; Hage, P.; Smit, Y.; de Winter, W.; Donker, J. Predicting Potential Aeolian Sand Supply to a High and Steep Foredune. In Proceedings of the AGU Fall Meeting Abstracts, Washington, DC, USA, 10–14 December 2018.
52. Bauer, B.O.; Davidson-Arnott, R.G.; Walker, I.J.; Hesp, P.A.; Ollerhead, J. Wind direction and complex sediment transport response across a beach–dune system. *Earth Surf. Process. Landf.* **2012**, *37*, 1661–1677. [CrossRef]
53. Davidson-Arnott, R.; Dawson, J. Moisture and fetch effects on rates of aeolian sediment transport, Skallingen, Denmark. In Proceedings of the Canadian Coastal Conference, Canadian Coastal Science and Engineering Association, Ottawa, ON, Canada, 5–9 November 2001; pp. 309–321.
54. Schmutz, P.; Briggs, T.; Tereszkiewicz, P. The utility of an omni-directional photoelectronic sensor device to measure meso-scale variability in aeolian sediment transport activity. *Aeolian Res.* **2019**, *36*, 61–67. [CrossRef]
55. Jackson, N.L.; Nordstrom, K.F. Aeolian sediment transport and landforms in managed coastal systems: A review. *Aeolian Res.* **2011**, *3*, 181–196. [CrossRef]
56. Delgado-Fernandez, I.; Jackson, D.W.; Cooper, J.A.G.; Baas, A.C.; Beyers, J.M.; Lynch, K. Field characterization of three-dimensional lee-side airflow patterns under offshore winds at a beach-dune system. *J. Geophys. Res. Earth Surf.* **2013**, *118*, 706–721. [CrossRef]
57. Donker, J.; van Maarseveen, M.; Ruessink, G. Spatio-temporal variations in foredune dynamics determined with mobile laser scanning. *J. Mar. Sci. Eng.* **2018**, *6*, 126. [CrossRef]
58. Hoonhout, B.M.; Vries, S.D. A process-based model for aeolian sediment transport and spatiotemporal varying sediment availability. *J. Geophys. Res. Earth Surf.* **2016**, *121*, 1555–1575. [CrossRef]